International Communications in Heat and Mass Transfer 173 (2026) 110802

Contents lists available at ScienceDirect

International Communications in Heat and Mass Transfer

journal homepage: www.elsevier.com/locate/ichmt

Thermal resistance analysis of cold-protective clothing using numerical modeling: Influence of natural-based nonwoven fabric structure and wind flow conditions

Seyyed Mohsen Mortazavinejad [a,*], Ludwig Vinches [b], Stéphane Hallé [a]

[a] Dept. of Mechanical Engineering, École de Technologie Supérieure, 1100 Notre-Dame West, Montreal, QC H3C 1K3, Canada
[b] Dept. of Environmental and Occupational Health, University of Montreal, 2375 Chemin. de La Côte-Sainte-Catherine, Montreal, QC H3T 1A8, Canada

ARTICLE INFO

Keywords:
Porous media
Fibrous structure
Heat transfer
Thermal insulation
Forced convection
Numerical modeling

ABSTRACT

Natural-based nonwovens featuring hollow fibers are promising for cold-protective clothing due to biodegradability and low thermal conductivity. However, their thermal behavior under varying wind intensities and orientations remains insufficiently understood. This study investigates heat-transfer mechanisms using a two-dimensional numerical model based on the porous media approach under local thermal equilibrium. To account for radiation, a radiative thermal conductivity term was integrated into the energy equation. The methodology employs a novel isolation technique: by simulating an impermeable textile zone while maintaining other transport properties, the coupled effects of conduction and radiation were separated from total heat transfer to quantify the convective contribution. The model was validated against experimental data; results show that increasing thickness is inefficient; a 2.18-fold thickness increase improved thermal resistance by only 9.9%. In contrast, reducing air permeability to levels mimicking a thin film yielded a 2.83-fold improvement by suppressing the convection that initially account for 86.2% of total heat transfer at 4 m/s. These findings indicate that controlling permeability is significantly more critical than increasing bulk for enhancing insulation. This work provides a rigorous framework for designing lightweight, high-performance thermal barriers where a balance between thermal protection and water vapor transmission is essential for cold-protective clothing.

1. Introduction

According to ISO 15743, cold temperatures are defined as those below 10 °C, a threshold frequently exceeded during Canadian winters [1]. Exposure to such conditions accelerates body heat loss, increasing the risk of hypothermia and frostbite, which can be life-threatening [2]. Therefore, preventing cold-related risks and preserving thermal balance depends on the use of well-designed cold-protective clothing, whose effectiveness is determined by its thermal insulation [3].

Effective thermal insulation is typically achieved through materials that retain air within a porous network, a defining characteristic of fibrous structures. Among fibrous assemblies, nonwovens are widely employed in cold-protective clothing to maintain optimal thermal comfort because of their high porosity, low density, and cost-effectiveness [4,5]. In nonwoven manufacturing, long fibers are randomly distributed and bonded through chemical, thermal, or mechanical methods to form a stable web [6–8]. Despite their versatility, most commercial nonwoven insulations are derived from mineral or fossil-based materials that, while inexpensive, are energy-intensive to produce, generate greenhouse gas emissions, and pose waste management challenges due to poor biodegradability [9–11]. In contrast, plant-based natural fibers have emerged as sustainable alternatives for thermal insulation nonwovens, offering abundance, renewability, biodegradability, and intrinsic carbon storage capacity [12,13]. Given these environmental advantages, attention must now turn to understanding and analyzing the thermal resistance of nonwovens composed of natural fibers.

The thermal behavior of nonwovens made of natural fibers is primarily governed by parameters such as fiber morphology (hollow or solid), fiber diameter, porosity, and thickness, which collectively determine their insulating capability [14–17]. To evaluate the heat-transfer behavior of natural-fiber nonwovens, experimental analysis is typically performed using standardized methods such as the guarded hot

Abbreviations: MW, Milkweed; PLA, polylactic acid; 2D, Two-dimensional domain; 3D, Three-dimensional domain.

* Corresponding author.
E-mail address: seyyed-mohsen.mortazavinejad.1@ens.etsmtl.ca (S.M. Mortazavinejad).

https://doi.org/10.1016/j.icheatmasstransfer.2026.110802

Available online 14 February 2026

Nomenclature

C	Inertial resistance factor (m^{-1})
c_p	Specific heat of air (J/kg·K)
d_i, d_o	Inner and outer fiber diameter (m)
K_P	Sample permeability without the film (m^2)
$K_{P,film}$	Sample permeability with the film (m^2)
k_{eff}	Effective thermal conductivity (W/m·K)
k_f	Thermal conductivity of air (W/m·K)
k_i	Thermal conductivity of the fiber component (W/m·K)
k_{rad}	Radiative thermal conductivity (W/m·K)
k_s	Thermal conductivity of the fiber (W/m·K)
$k_{s,a}$	Axial thermal conductivity of the hollow fiber (W/m·K)
$k_{s,t}$	Transverse thermal conductivity of the hollow fiber (W/m·K)
L	Sample thickness (m)
p	Pressure (Pa)
q	Heat flux at the bottom of the hot-plate (W/m^2)
R	Thermal resistance (m^2·K/W)
T	Temperature (K)
$T_{reversed}$	Reversed flow air temperature (K)
$T_{zone\ 1}$	Zone 1 textile side temperature (K)
$T_{zone\ 2}$	Zone 2 textile side temperature (K)
t	Wall thickness of the fiber (m)
U_{in}, V_{in}	Velocity inlet for horizontal and vertical configuration (m/s)
u, v	Air velocity in x, y direction (m/s)
v_i	Volume fraction of each fiber component
x, y	Space coordinates

Greek symbols

ρ	Air density (kg/m^3)
ρ_{bulk}	Bulk density of the nonwoven sample (kg/m^3)
ρ_f, ρ_w	Fiber and wall density (kg/m^3)
ε	Total porosity of the nonwoven sample
$\varepsilon_i, \varepsilon_o$	Inner and outer porosity of the nonwoven sample
μ	Air viscosity (N·s/m^2)
μ_{eff}	Effective viscosity (N·s/m^2)
μ_r	Relative viscosity (N·s/m^2)
ϵ	Emissivity of the boundary surfaces
σ	Stefan Boltzmann constant ($W/m^2 \cdot K^4$)

plate or heat flow meter [18]. However, to better understand how fiber morphology, porosity, and thickness interact, theoretical and numerical modeling approaches are often employed to complement these measurements.

Owing to their highly porous structure, nonwoven fabrics contain a large fraction of still air, which dominates their insulating performance. In natural hollow fibers, this effect is further enhanced, as air trapped both between and within fibers provides additional resistance to heat transfer. However, a higher air fraction can also increase radiative heat transfer, as infrared radiation passes more easily through the porous medium [14]. Despite this, conduction remains the primary heat-transfer mechanism in highly porous fibrous assemblies [19]. Under windy conditions, airflow through the fabric induces forced convection within the porous network, making air a double-edged factor, advantageous for insulation under still wind flow but a source of convective heat loss when exposed to wind [20].

Several studies have attempted to investigate convective heat transfer within fibrous structures. Zhu et al. [21] modeled a simplified flat plate with multiple pores to study air penetration through fabrics, though the criteria used to define pore number and size were not clearly explained, leaving uncertainty about the model's representativeness. Another study applied the unit-cell approach under laminar flow to compare nonwoven fabrics with and without aerogel treatment, showing that aerogel-coated samples achieved up to 67% higher thermal resistance due to the nano porous structure of aerogel, which effectively trapped air and hindered heat flow [22]. A separate numerical analysis of fibrous packed beds reported that increasing fiber diameter from 8 to 14 mm reduced the average pressure gradient by about 77%, thereby enhancing overall heat transfer efficiency [23]. Tu et al. [24] developed a computational model of cold-protective clothing composed of a thin windproof outer layer and a thick insulation layer, demonstrating that lower outer-layer permeability reduced internal air movement and convective heat loss, while a less permeable inner layer improved thermal insulation. Similarly, when porous textiles were covered with a windproof layer, their insulation remained almost constant across windy conditions, indicating minimal influence of ambient airflow [25]. In another work, Tu et al. [26] proposed a model to evaluate the thermal resistance of textile ensembles, showing that conduction dominated in low-porosity fabrics, and convective resistance decreased sharply with higher wind velocity and air permeability. Although these studies advanced the understanding of airflow and heat-transfer behavior within porous textiles, none clearly quantified the relative contributions of conduction and convection, and the radiative component was entirely neglected. In the work of Shen et al. [20], an attempt was made to distinguish between conductive and convective effects; however, the methodology was only briefly outlined, leaving some aspects open to interpretation, and left some uncertainty regarding its implementation. Moreover, the thermophysical characterization in this study relied on the effective thermal conductivity of the overall fabric sample, without addressing how the intrinsic thermal conductivities of individual fibers influenced the results.

The existing literature reveals several critical research gaps, which are summarized below. Specifically, the integration of multi-component fiber blends into the energy equation is often oversimplified, and the specific impact of fiber hollowness on heat transfer mechanisms is rarely addressed. Furthermore, limited comparative data exist regarding how wind orientation, specifically horizontal versus vertical exposure affects thermal resistance. Most notably, there is a lack of rigorous methodology capable of quantitatively separating the individual contributions of conduction, convection, and radiation within such complex porous structures.

Building upon these gaps, this numerical study systematically investigates the thermal performance of multi-component nonwoven assemblies composed of kapok, milkweed (MW), and polylactic acid (PLA). The selection of these fibers was guided by industrial partner relevance, local availability, and advantageous physical properties [26,27]. Unlike previous research, this work employs a novel methodology to isolate the roles of conduction, convection, and radiation under varying wind orientations. The governing parameters, including fabric thickness and air permeability, are examined to determine their collective influence on overall insulation. To ensure model reliability, the numerical findings are validated against experimental data obtained from the developed bench test. Ultimately, this study provides a comprehensive understanding of the mechanisms governing heat transfer in natural-fiber nonwovens for cold-protective applications.

2. Method and modeling framework

2.1. Materials

Three nonwoven fabric structures (denoted S1, S2, and S3) were investigated in this study. Each structure consisted of a blend of 50%

solid PLA fibers, providing structural stability, and 25% hollow kapok and 25% hollow MW fibers, which contributed to enhanced thermal insulation. This balance arises from the distinct roles of the fibers: the solid PLA component ensures mechanical stability, while the naturally hollow kapok and MW fibers reduce solid conduction pathways, thereby improving thermal resistance. To substantiate these characteristics, scanning electron microscopy images confirmed the hollow morphology of kapok and MW fibers, whereas PLA fibers were observed to be solid [19].

The resulting nonwoven fabrics (S1–S3) varied primarily in areal density and thickness: S1 was the lightest, S2 exhibited intermediate areal density and thickness, and S3 was the thickest. Despite these variations, all three maintained a consistently high porosity (> 99%), a feature typical of natural fiber-based insulations [14]. Their detailed characteristics are summarized in Table 1, which reports areal density, thickness (L), bulk density (ρ_{bulk}), and the inner (ε_i), outer (ε_o), and total porosities (ε), coupled with the measured air permeability values. Since all three fabrics were laminated with a thin cotton film, permeability was assessed under two conditions, with the film ($K_{P,film}$) and without the film (K_P), to capture the influence of the cover layer.

Additionally, the geometric and thermophysical properties of the three fibers are presented in Table 2. The reported values include inner fiber diameter (d_i), wall thickness (t), fiber and wall densities (ρ_f and ρ_w), and thermal conductivity (k_s). For kapok and MW, which are hollow fibers, the table also lists the axial ($k_{s,a}$) and transverse ($k_{s,t}$) thermal conductivities, providing insight into their anisotropic behavior. Detailed descriptions of the measurement procedures and calculation methodologies used to obtain these parameters are available in one of our earlier studies [19].

Having established the composition and structural characteristics of the fibers and nonwoven fabrics, the next step was to experimentally evaluate their thermal resistance under controlled conditions.

2.2. Experimental setup for thermal resistance measurement

The thermal resistance of the nonwoven fabric structures was evaluated using a guarded hot plate (skin model) apparatus previously developed and validated in the earlier work [28]. The system consists of independently regulated heating zones that maintain the measuring hot plate at 35 ± 0.2 °C, while the surrounding chamber is controlled at 20 ± 1 °C and 65 ± 5% relative humidity, following the ISO 11092 standard [29]. The hot plate dimensions were 30.48 × 30.48 cm, and the textile specimens were trimmed to match the surface area. The method has been benchmarked against independent laboratory results, showing deviations of less than 5%, thereby confirming its accuracy and reliability.

Before measurement, each sample was conditioned for 24 h at 20 °C and 65% relative humidity. To ensure reproducibility, three replicate tests were then conducted. For each test, data acquisition began once steady-state conditions were reached, and measurements were recorded over a 20-min period at a rate of one reading per second.

Heat transmission across the nonwoven assemblies takes place in two stages. Within the bulk of the fabric, heat transfers through conduction, radiative exchange between fibers, and forced convection. Previous studies have shown that natural convection is negligible in typical fibrous insulation materials [30,31]. At the outer boundary, heat is released mainly through convection at the exposed top surface, as the lateral edges were sealed with tape to minimize side losses. Because of the high porosity and air permeability of the textiles, externally applied airflow could readily penetrate the structure, making wind effects particularly important. To capture this influence, airflow was introduced at three velocities: 1, 2, and 4 m/s.

The effect of wind orientation was also investigated. In the horizontal configuration, air was supplied through an inlet positioned 12 cm from the hot plate, whereas in the vertical configuration, airflow entered from

Table 2
Geometric and thermophysical properties of kapok, MW, and PLA fibers [19].

Fiber	d_i (μm)	t (μm)	ρ_w (kg/m^3)	ρ_f (kg/m^3)	k_s (W/m·K)	$k_{s,a}$ (W/m·K)	$k_{s,t}$ (W/m·K)
kapok	24.05 ± 2.62	0.84 ± 0.38	1553.4 ± 24.7	196.9	0.250	0.054	0.056
MW	24.95 ± 3.87	1.03 ± 0.40	1721.0 ± 41.4	252.3	0.307	0.067	0.066
PLA	15.02 ± 2.19	–	1277.0 ± 3.3	1277.0	0.263	–	–

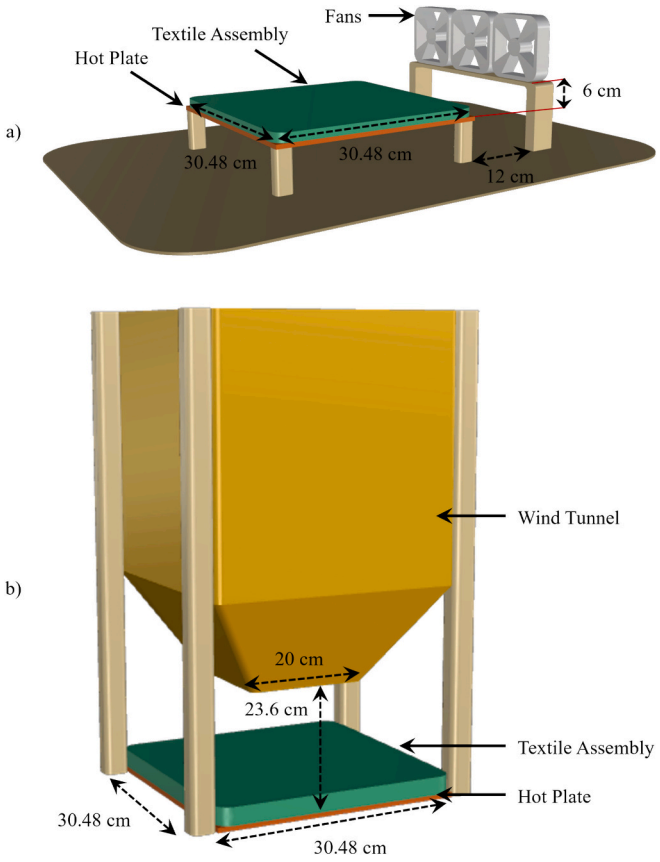

Fig. 1. Schematic of the experimental setup for thermal resistance measurement under horizontal (a) and vertical (b) wind orientations adapted from [28].

Table 1
Key properties of the nonwovens [19].

Sample ID	Areal Density (gsm)	Area (mm^2)	L (mm)	ρ_{bulk} (kg/m^3)	ε_i (%)	ε_o (%)	ε (%)	$K_{P,film}$ (× 10^{-7} m^2)	K_P (× 10^{-7} m^2)
S1	108.53	106,534.70	10.20	10.640	2.080	97.385	99.466	0.089	1.818
S2	147.61	98,158.33	15.70	9.402	1.838	97.690	99.528	0.194	2.155
S3	250.13	99,562.67	22.30	11.216	2.193	97.244	99.437	0.192	2.090

an opening located 23.6 cm above the hot plate. Schematic diagrams of these two arrangements are provided in Fig. 1-a (horizontal) and Fig. 1-b (vertical).

Thermal resistance (R) in m^2·K/W was calculated from the measured heat flux (q) and the temperature difference (ΔT) between the hot plate and the ambient air, according to Eq. (1). The resulting values were converted into clo units by multiplying by 0.155, where 1 clo corresponds to the thermal insulation required for a person at rest to remain comfortable in a 21 °C environment with 50% relative humidity [32]. A complete description of the apparatus design and calculation methodology can be found in the earlier study [28].

$$R = \frac{\Delta T}{q} \tag{1}$$

Building on these experimental setups, the next step was to establish a numerical modeling framework to simulate heat transfer in the nonwoven fabrics; therefore, in the following section, the computational domain and governing equations are presented to capture the influence of horizontal and vertical wind flow orientations.

2.3. Numerical modeling

2.3.1. Computational domain and boundary conditions

Unlike the three-dimensional (3D) computational domains used by Shen et al. [20] to investigate the thermal resistance of nonwoven structures, the present study adopted a two-dimensional (2D) domain. This decision was motivated by the use of a porous medium model for the textile zone, in which the governing equations incorporated structure-specific parameters such as air permeability in the momentum equations and effective thermal conductivity in the energy equation. Within this consideration, the actual fiber arrangement inside the porous zone did not need to be explicitly resolved, as would have been required in a 3D real porous model with randomly distributed fibers [23]. Instead, the porous medium approach allowed the textile to be represented as a simplified rectangular region, which captured the bulk transport behavior while significantly reducing computational cost. Consequently, extending the analysis to 3D would not have improved accuracy but would have substantially increased computational demand. The rectangular textile zone was defined with its width equal to the fabric thickness, while the overall length of the computational domain was extended to twice the textile dimension in the streamwise direction for the horizontal configuration and in both directions for the vertical configuration. This enlargement of the domain ensured that the imposed boundary conditions at the outer edges did not interfere with the flow or thermal fields around the textile. Because the external airflow interacted with the textile, an enclosure was introduced to represent the inlet region. To further limit computational cost, a slip-wall boundary condition was applied at the outer edge of the enclosure rather than extending the computational domain to far boundaries.

Boundary conditions were assigned as follows: the bottom surface of the textile was maintained at a constant temperature of 35 °C and treated as a no-slip wall. The lateral edges of the textile were set to impermeable to suppress side losses, while the top boundary allowed convective exchange with the external flow. For the vertical orientation case, symmetry in the geometry permitted the use of a symmetry boundary condition, such that only half of the domain needed to be simulated.

Because three distinct fabric structures (S1–S3) were studied under both horizontal and vertical wind orientations, a total of six computational domains were constructed. The detailed boundary conditions for each configuration are summarized in Table 3. These include the inlet velocities (U_{in}, V_{in}) for horizontal and vertical configuration, the backflow temperature for potential reversed flow ($T_{reversed}$), and the textile side temperatures for Zone 1 and Zone 2 ($T_{zone\ 1}$ and $T_{zone\ 2}$). Representative computational domain schematics illustrating these arrangements and zones are provided in Fig. 2.

Table 3
Boundary conditions for the computational domains under horizontal and vertical wind orientations.

Configuration	Boundary	Condition	Mathematical formulation
Horizontal	Inlet	Velocity inlet	$u = U_{in}; v = 0; T = 20^{\circ}C$
	Outlet	Pressure outlet	$p = 0; T_{reversed} = 20^{\circ}C$
	Top, Bottom	Slip wall	$\frac{\partial u}{\partial y} = 0; v = 0; T = 20^{\circ}C$
	Bottom-textile	No-slip wall	$u = v = 0; T = 35^{\circ}C$
	Left-textile, Right-textile	Coupled	$u = v = 0; T_{zone\ 1} = T_{zone\ 2}; k_f \cdot \frac{\partial T_{zone\ 1}}{\partial x} = k_{eff} \cdot \frac{\partial T_{zone\ 2}}{\partial x}$
Vertical	Inlet	Velocity inlet	$u = 0; v = V_{in}; T = 20^{\circ}C$
	Outlet	Pressure outlet	$p = 0; T_{reversed} = 20^{\circ}C$
	Top, Bottom	Slip wall	$\frac{\partial u}{\partial y} = 0; v = 0; T = 20^{\circ}C$
	Bottom-textile	No-slip wall	$u = v = 0; T = 35^{\circ}C$
	Left-textile	Coupled	$u = v = 0; T_{zone\ 1} = T_{zone\ 2}; k_f \cdot \frac{\partial T_{zone\ 1}}{\partial x} = k_{eff} \cdot \frac{\partial T_{zone\ 2}}{\partial x}$
	Right	Symmetry	$u = 0; \frac{\partial v}{\partial x} = 0; \frac{\partial p}{\partial x} = 0; \frac{\partial T}{\partial x} = 0$

With the computational domain and boundary conditions established, the next step was to present the governing equations and modeling assumptions applied to both the porous textile region and the surrounding airflow domain.

2.3.2. Modeling assumptions and governing equations

To develop the numerical model, several assumptions were made. The analysis was limited to steady-state conditions, as transient effects with fluctuating heat flux were beyond the scope of this study. The airflow was assumed incompressible, justified by a maximum wind velocity of 32 m/s corresponding to a Mach number below 0.3. Additionally, the thermophysical properties of both the fibers and the air were considered temperature-independent, given the small temperature gradients applied in the simulations. Under these assumptions, fluid flow and heat transfer in the computational domain were governed by the 2D Navier–Stokes equations for continuity, momentum, and energy conservation. As illustrated in Fig. 2, two zones were defined: Zone 1, representing the external airflow over the textile, and Zone 2, representing the airflow through the porous fabric.

Because of the strong wind imposed on the system, the external flow within Zone 1 was modeled as turbulent, while the internal flow in Zone 2 was treated as laminar, reflecting the pressure drop induced by the fibrous structure [20]. For Zone 1, the governing equations (Eqs. (2)–(5)) were solved using the Reynolds-averaged Navier–Stokes formulation, in which the flow variables are decomposed into mean and fluctuating components (e.g., $u = \bar{u} + u', v = \bar{v} + v', p = \bar{p} + p'$ and $T = \bar{T} + T'$). The turbulence was then modeled using the k–ω shear-stress transport (SST) approach, which provides a reliable formulation for capturing near-wall behavior and convective heat transfer in external flows [33]. This model is particularly advantageous for wall-bounded flows due to its hybrid nature; it blends the robust k–ω formulation in the near-wall region with the k–ε model in the far-field. Such an approach is critical for accurately resolving the boundary layer development on the textile surface, which directly governs the convective heat transfer mechanisms.

Continuity equation:

$$\frac{\partial \bar{u}}{\partial x} + \frac{\partial \bar{v}}{\partial y} = 0 \tag{2}$$

Momentum equation (x direction):

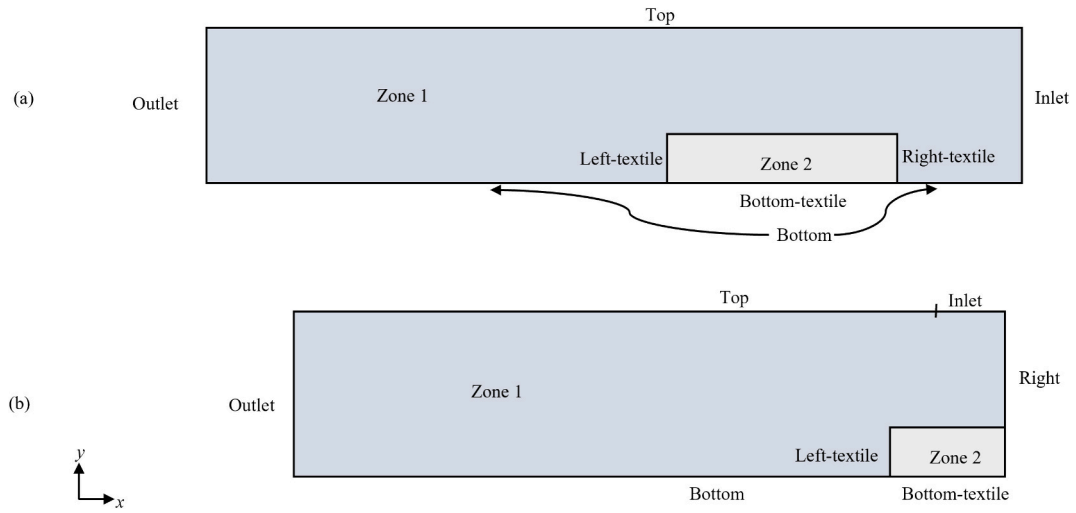

Fig. 2. Representative computational domains for thermal resistance analysis of nonwoven fabrics under (a) horizontal and (b) vertical wind orientations.

$$\bar{u}\frac{\partial \bar{u}}{\partial x}+\bar{v}\frac{\partial \bar{u}}{\partial y}=-\frac{1}{\rho}\frac{\partial \bar{p}}{\partial x}+\frac{\mu}{\rho}\left(\frac{\partial^2 \bar{u}}{\partial x^2}+\frac{\partial^2 \bar{u}}{\partial y^2}\right)-\left(\frac{\partial(u'u')}{\partial x}+\frac{\partial(u'v')}{\partial y}\right) \tag{3}$$

Momentum equation (y direction):

$$\bar{u}\frac{\partial \bar{v}}{\partial x}+\bar{v}\frac{\partial \bar{v}}{\partial y}=-\frac{1}{\rho}\frac{\partial \bar{p}}{\partial y}+\frac{\mu}{\rho}\left(\frac{\partial^2 \bar{v}}{\partial x^2}+\frac{\partial^2 \bar{v}}{\partial y^2}\right)-\left(\frac{\partial(u'v')}{\partial x}+\frac{\partial(v'v')}{\partial y}\right) \tag{4}$$

Energy equation:

$$\bar{u}\frac{\partial \bar{T}}{\partial x}+\bar{v}\frac{\partial \bar{T}}{\partial y}=\frac{k}{\rho c_p}\left(\frac{\partial^2 \bar{T}}{\partial x^2}+\frac{\partial^2 \bar{T}}{\partial y^2}\right)-\left(\frac{\partial(u'T')}{\partial x}+\frac{\partial(v'T')}{\partial y}\right) \tag{5}$$

The turbulence intensity at the domain inlet was prescribed based on laboratory measurements and the definitions given in ASHRAE 55 [34]. In this standard, turbulence intensity is defined as the ratio of the standard deviation of the velocity fluctuations to the mean velocity. Experimental airspeed data from the fan were processed to determine the mean velocity and its fluctuations, and the resulting turbulence intensity values for each wind orientation were then applied as boundary conditions. The assigned values are summarized in Table 4.

In Zone 2, the porous structure of the fibrous material was modeled as a homogeneous porous region, where part of the external air penetrated the textile. To capture this effect, a momentum sink term was added to the laminar fluid flow equations, representing the pressure drop caused by the fibrous network resisting airflow penetration and effectively coupling the porous material to the flow field, as expressed in Eq. (6) [31].

$$\begin{cases} S_x=-\left(\dfrac{\mu}{K_P}u+\dfrac{Cu}{2}\rho\sqrt{u^2+v^2}\right) \\ S_y=-\left(\dfrac{\mu}{K_P}v+\dfrac{Cv}{2}\rho\sqrt{u^2+v^2}\right) \end{cases} \tag{6}$$

Here, S_x and S_y denote the momentum sink terms in the x and y directions, respectively. K_P represents the air permeability of the porous structure, u and v are the velocity components in the x and y directions, and C is the inertial resistance factor. The first term on the right-hand side of each equation corresponds to viscous losses, while the second term represents inertial resistance. In the present study, the airflow within the porous region was assumed to be laminar, as the internal air velocity was sufficiently low. Under these conditions, inertial loss was neglected, thereby reducing Eq. (6) to Darcy's law, expressed by Eq. (7) [35,36].

$$\begin{cases} S_x=-\dfrac{\mu}{K_P}u \\ S_y=-\dfrac{\mu}{K_P}v \end{cases} \tag{7}$$

To account for the effect of the film layer covering the textile samples, the sink term in the y direction was modified. Specifically, K_P was replaced by $K_{P,film}$, to represent the additional resistance introduced by the film, since its influence acts only normal to the fabric plane and not along its length. Under this framework, the momentum equations were solved for the fluid region with direction-dependent sink terms. The resulting governing equations in the x and y directions can therefore be expressed as Eqs. (8) and (9).

Momentum equation (x direction):

$$u\frac{\partial u}{\partial x}+v\frac{\partial u}{\partial y}=-\frac{1}{\rho}\frac{\partial p}{\partial x}+\frac{\mu}{\rho}\left(\frac{\partial^2 u}{\partial x^2}+\frac{\partial^2 v}{\partial y^2}\right)-\frac{\mu_{eff}}{K_P}u \tag{8}$$

Momentum equation (y direction):

$$u\frac{\partial v}{\partial x}+v\frac{\partial v}{\partial y}=-\frac{1}{\rho}\frac{\partial p}{\partial y}+\frac{\mu}{\rho}\left(\frac{\partial^2 v}{\partial x^2}+\frac{\partial^2 v}{\partial y^2}\right)-\frac{\mu_{eff}}{K_{P,film}}v \tag{9}$$

Eq. (10) defines the effective viscosity (μ_{eff}), incorporating the relative viscosity (μ_r) determined via the Brinkman correction in Eq. (11) [37]:

$$\mu_{eff}=\mu\mu_r \tag{10}$$

$$\mu_r=(1-\varepsilon_o)^{-2.5} \tag{11}$$

It is noted that while the original formulation utilizes total porosity (ε), the outer porosity (ε_o) was employed in Eq. (11). This substitution was implemented to explicitly integrate the effect of fiber hollowness into the effective viscosity calculation.

For the energy transport within the textile, a local thermal equilibrium model was adopted. This approach assumes that the solid fibers and the air share the same temperature ($T_s = T_f = T$). As a result, convective heat exchange between the fibers and air is neglected. Benefiting from the local thermal equilibrium approach is justified by

Table 4
Mean velocity and turbulence intensity values.

Horizontal	Velocity (m/s)	1	2	4
	Mean velocity (m/s)	1.11	2.08	3.91
	Turbulence intensity (%)	6.16	6.65	3.95
Vertical	Velocity (m/s)	1	2	4
	Mean velocity (m/s)	1.11	2.02	4.18
	Turbulence intensity (%)	5.12	7.71	4.70

the significant difference between volumetric heat capacity of solid and fluid phases. The solid fibers possess a substantially higher heat capacity than the interstitial air, effectively functioning as a dominant thermal reservoir. Consequently, the air within the porous structure rapidly adjusts to the temperature of the surrounding fibers. This phenomenon results in a negligible temperature difference between the solid and fluid phases, thereby validating the use of this approach. Considering this, the porous region is represented by a single effective energy equation, expressed as Eq. (12) [31].

$$u\frac{\partial T}{\partial x}+v\frac{\partial T}{\partial y}=\frac{k_{eff}}{\rho c_p}\left(\frac{\partial^2 T}{\partial x^2}+\frac{\partial^2 T}{\partial y^2}\right) \tag{12}$$

The effective thermal conductivity (k_{eff}) in Eq. (12) is a function of both the porosity (ε) and the thermal conductivities of the fibers and air (k_s, k_f). Although various models have been proposed in the literature to account for fiber arrangement, in the case of highly porous insulation materials ($\varepsilon \approx 99\%$), fiber orientation has only a negligible effect on k_{eff} [19]. Therefore, the simplest expression for effective thermal conductivity was adopted in the present study, calculated by Eq. (13).

$$k_{eff}=\varepsilon k_f+(1-\varepsilon)k_s \tag{13}$$

However, some adjustments were required in the application of Eq. (13) for calculating k_{eff}. Specifically, the original form of this equation was developed under the assumption of a single solid fiber type, whereas in the present study the fabric structure consisted of three different fibers. To address this, the average thermal conductivity of the fiber mixture was determined using Eq. (14), in which the weighting factor x_i is calculated from Eq. (15) based on the volume fraction (v_i) of each fiber component [38].

$$k_s=\sum_{i=1}^{n=3} x_i \times k_i \tag{14}$$

$$x_i=\frac{v_i}{\sum_{i=1}^{n=3} v_i} \tag{15}$$

Also, among the fibers considered, kapok and MW possess a hollow structure, and their hollowness must be accounted for in the thermal conductivity calculation. This was achieved by incorporating both axial and transverse conductivities ($k_{s,a}$ and $k_{s,t}$) when formulating Eq. (14); therefore, the values of thermal conductivity for kapok and MW were adjusted accordingly. With this adjustment, Eq. (14) was reformulated as Eq. (16), where the representative values for each fiber are provided in Table 2.

$$k_s=x_{kapok}\left(0.5k_{kapok,a}+0.5k_{kapok,t}\right)+x_{MW}\left(0.5k_{MW,a}+0.5k_{MW,t}\right)+x_{PLA}k_{PLA} \tag{16}$$

Also, in Eq. (13), the total porosity (ε) was replaced by the outer porosity (ε_o). This adjustment was necessary because the effect of hollowness and inner porosity (ε_i) caused by kapok and MW is already embedded in the calculation of k_s using Eq. (14). Therefore, only ε_o, which determines the fraction of air between fibers in the composite, should be considered in the effective conductivity model. With this modification, Eq. (13) can be reformulated as Eq. (17), where k_s now represents the averaged thermal conductivity of the fiber blend, calculated using Eq. (16). The detailed derivation and justification for these modifications are presented in the earlier work [19].

$$k_{eff}=\varepsilon_o k_f+(1-\varepsilon_o)k_s \tag{17}$$

The effect of radiation between fibers was incorporated into the effective thermal conductivity as a radiative term, k_{rad}, based on the Rosseland model [39,40]. In this study, rather than performing detailed spectral characterization, k_{rad} was approximated using the simplified expression proposed in the study done by Farnworth [41]. This approach, which assumes that radiation occurs primarily between nearly opaque fibers, eliminates the need for direct transmittance evaluation. Therefore, k_{rad} can be expressed using Eq. (18) [41]:

$$k_{rad}=\frac{4\sigma T^3 d_o}{(1-\varepsilon)\epsilon} \tag{18}$$

In this approximation, T represents the temperature of the fabric structure, ϵ is the emissivity of the boundary surfaces, and d_o is the outer fiber diameter, which in the present case was taken as the mean outer diameter of the constituent fibers. To calculate d_o , the necessary parameters for wall thickness and inner diameter are listed in Table 2. Since the model was originally developed for single solid fibers, the term ε should be replace with ε_o, to properly account for the effect of hollowness in kapok and MW fibers. With these adjustments, the effective thermal conductivity of the porous region was expressed as the sum of conductive and radiative contributions, as shown in Eq. (19):

$$k_{eff}=\varepsilon_o k_f+(1-\varepsilon_o)k_s+\frac{4\sigma T^3 d_o}{(1-\varepsilon_o)\epsilon} \tag{19}$$

By modifying the k_{eff} term in Eq. (12) with the expression given in Eq. (19), the combined effects of conduction and radiation in the porous zone were captured simultaneously. This formulation allowed the evaluation of both mechanisms within a unified framework. Having established the governing equations and boundary conditions, the next step was to describe how these equations were discretized and solved.

2.3.3. *Numerical implementation: grid, discretization, and solution strategy*

As noted in the description of the computational domain, six distinct configurations were required to account for the three fabric structures (S1–S3) under both horizontal and vertical wind orientations. For each configuration, grid resolution was examined by generating coarse, medium, and fine grids, with the corresponding number of elements summarized in Table 5. A structured quadrilateral mesh was employed in all cases, and the grids were generated using the ANSYS meshing tool.

The simulations were carried out using ANSYS Fluent 20.2, which applies the finite volume method to discretize and solve the governing equations. The coupling between velocity and pressure fields was resolved using the coupled algorithm. For pressure discretization, the Pressure Staggering Option (PRESTO) scheme was employed. Diffusion and convection terms in the momentum equations were discretized using the second-order upwind scheme, and the same second-order upwind approach was also applied to the turbulence kinetic energy, dissipation rate, and energy equations. To ensure numerical accuracy, the convergence criterion for the energy equation was set to 10^{-6}, while for all other governing equations it was set to 10^{-5}.

One of the most important aspects of the present study is the methodology developed to isolate the contributions of conduction, convection, and radiation to the overall heat transfer in fibrous porous media. After solving the governing equations, the average heat flux at the bottom surface of the textile assembly was obtained numerically. This value was directly compared with the experimentally measured heat flux (described in Section 2.2), thereby providing a means of validating the numerical approach.

In the literature, no clear framework exists for distinguishing

Table 5
Number of elements for coarse, medium, and fine grid resolutions of the nonwoven structures.

Configuration	Grid resolution	Number of elements S1	Number of elements S2	Number of elements S3
Horizontal	Coarse	36,504	44,460	47,532
	Medium	74,580	87,120	95,040
	Fine	150,080	176,344	193,228
Vertical	Coarse	32,927	36,820	40,502
	Medium	66,600	72,520	79,920
	Fine	134,656	146,228	160,956

conduction, convection, and radiation in porous fibrous materials; however, the average heat flux calculated by numerical modeling inherently represents their combined effect. In this study, a systematic procedure was introduced. Because the energy equation was solved under the local thermal equilibrium assumption, convective heat exchange between fibers and air was omitted; thus, any convective contribution originates solely from the airflow penetrating the porous structure.

To quantify this effect, the total average heat flux, q, was first expressed in terms of the effective thermal conductivity (k_{eff}) from Eq. (19) and the applied temperature gradient ($\frac{\partial T}{\partial y}$) at the bottom of the textile, as expressed by Eq. (20):

$$q = k_{eff}\frac{\partial T}{\partial y} \tag{20}$$

If the textile were treated as impermeable, i.e., with airflow inside the porous zone suppressed by setting the velocity components in both x and y directions to zero, the resulting heat flux would represent only conduction and radiation. In this case, the conduction and radiation components were further separated by scaling the two terms in Eq. (19), based on the respective contributions of conductive and radiative thermal conductivity.

Finally, the convective component was isolated by subtracting the conduction coupled with radiation flux (impermeable case) from the total flux obtained under real conditions with airflow penetration. In this way, the individual contributions of conduction, convection, and radiation were systematically determined. This approach provides a practical framework for decoupling heat transfer mechanisms in fibrous porous media.

3. Results and discussions

In this section, the numerical model was first assessed for grid independence to ensure that mesh resolution had no influence on the numerical results. Then, they were validated against experimental measurements for one representative fabric sample, confirming the reliability of the simulation approach. Following validation, the influence of fabric thickness on thermal resistance was examined under different wind velocities. The analysis then extended to quantify the relative contributions of conduction, convection, and radiation for each structure under both horizontal and vertical flow orientations. Finally, a detailed investigation was conducted to evaluate how increasing the inlet air velocity and modifying the fabric air permeability influence the overall thermal resistance of the nonwoven assemblies.

3.1. Grid independence study

Grid independence was evaluated for each fabric sample (S1–S3) and both wind orientations (horizontal and vertical), following the meshing framework in Section 2.3.3. Sample S1 was used as a representative case. At the highest inlet velocity, considered the most critical condition, the total heat flux was compared across coarse, medium, and fine grids. As shown in Table 6, the variations in total heat flux between consecutive grid levels (coarse–medium and medium–fine) were evaluated for both configurations, with the change between the medium and fine grids being 0.62% and 0.63% for the horizontal and vertical cases, respectively, confirming mesh independence.

Table 6
Value and change in total heat flux across successive grid refinements for horizontal and vertical configurations (S1 sample).

Configuration	Grid resolution	Total heat flux	
		Value (W/m^2)	Change (%)
Horizontal	Coarse	73.61	–
	Medium	72.80	1.11
	Fine	72.35	0.62
Vertical	Coarse	185.04	–
	Medium	183.06	1.08
	Fine	181.91	0.63

For S2 and S3, similar analyses were performed. The change in total heat flux between the medium and fine grids was below 0.21% (horizontal) and 0.59% (vertical) for S2, and 0.83% (horizontal) and 0.60% (vertical) for S3. Therefore, the medium grid resolution was adopted for all subsequent simulations as it ensured accurate yet computationally efficient results.

3.2. Model validation and flow behavior inside the textile

The numerical model was validated by comparing simulated heat flux values with experimental measurements for sample S2, adapted from the previously published work [28]. As presented in Fig. 3(a–b), the experimental error bars provide a comprehensive representation of inaccuracy by incorporating both propagated measurement uncertainties, quantified from instrument specifications, and repeatability errors (standard deviation). The maximum deviation between the numerical and experimental results was approximately 18.6% for the horizontal configuration and 20.2% for the vertical one, demonstrating good overall agreement and confirming the reliability of the developed model. The remaining differences can be attributed partially to the assumption of local thermal equilibrium within the porous domain, where the temperature difference between the fibers and the air in each computational cell is neglected. This simplification tends to underestimate the total heat flux, particularly evident in Fig. 3 (a). Furthermore, the discrepancies can also be explained by the use of a 2D model, considering that turbulent flow structures are inherently 3D in nature. Additional discrepancies may arise from the use of a porous-media representation instead of an explicitly resolved fibrous geometry, as well as structural nonuniformities inherent to the manufacturing process. During fabrication, local variations in fiber packing density may occur, such as fiber accumulation in some regions and sparse distribution in others, altering the airflow pathways through the textile.

Despite these factors, the model accurately reproduced experimental trends, with deviations as low as 7.1% for a vertical flow of 2 m/s and 6.4% for a horizontal flow of 1 m/s. These results confirm that the numerical framework provides a reliable and physically consistent prediction of the thermal behavior of nonwoven fabrics under varying wind conditions.

Fig. 4(a–b) presents the temperature contours for sample S2 at an inlet velocity of 4 m/s under horizontal and vertical flow orientations. The results reveal a more extensive air penetration in the vertical configuration, as a larger portion of the textile domain exhibits temperatures approaching the ambient value. This observation is supported by the mean thermal data at the textile's top surface: the horizontal case shows a higher mean temperature of 293.73 K and a steeper mean temperature gradient ($\frac{\partial T}{\partial y} \approx 469.9$ K/m), whereas the vertical configuration exhibits a lower mean temperature of 293.24 K and a much smaller gradient ($\frac{\partial T}{\partial y} \approx 69.8$ K/m), indicating reduced thermal insulation and stronger convective heat transfer within the fabric. The corresponding velocity vectors in Fig. 5(a–b) confirm this trend, showing a higher internal flow intensity for the vertical case. The mean velocity entering the textile zone in the vertical orientation was approximately 1.402 m/s, compared with 0.493 m/s in the horizontal case, about 2.8 times higher, demonstrating the greater ease of airflow penetration in the vertical setup.

3.3. Effect of the fabric thickness on thermal resistance of the samples

The influence of fabric thickness on thermal resistance is illustrated in Fig. 6 (a–c) for inlet velocities of 1, 2, and 4 m/s under both horizontal and vertical wind orientations. When the airflow velocity is low (1 m/s)

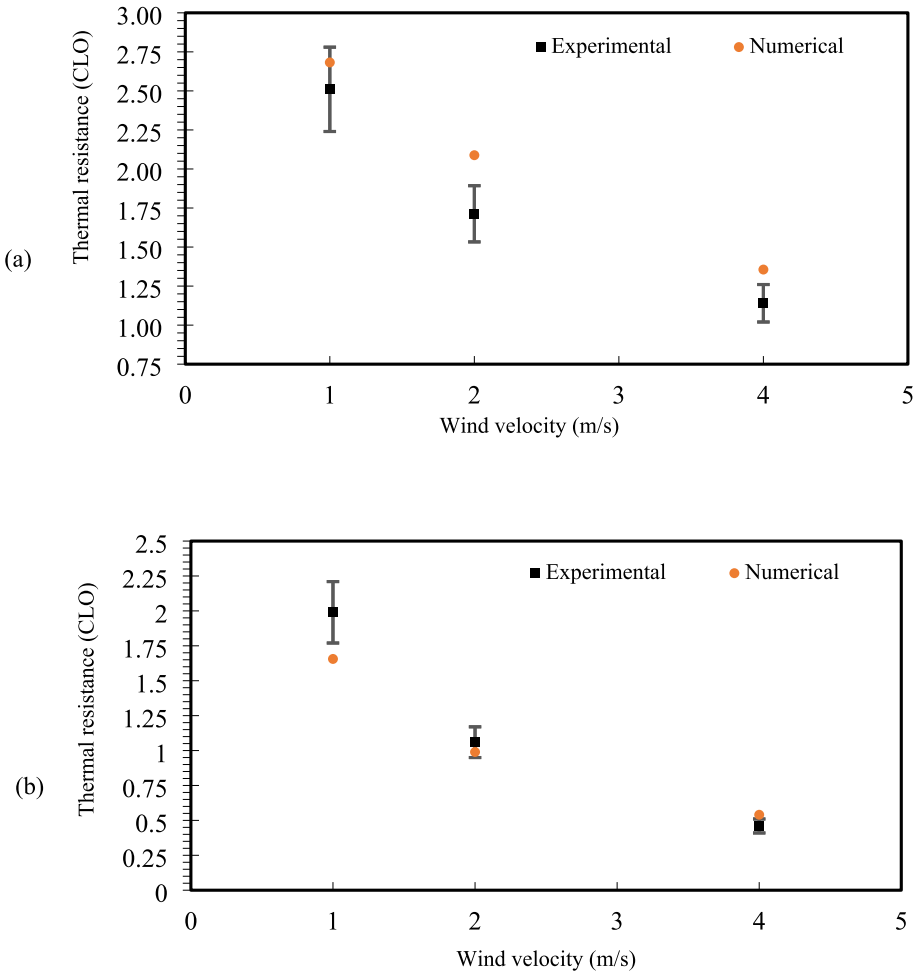

Fig. 3. Comparison of experimental and numerical heat flux for sample S2 under (a) horizontal and (b) vertical wind orientations.

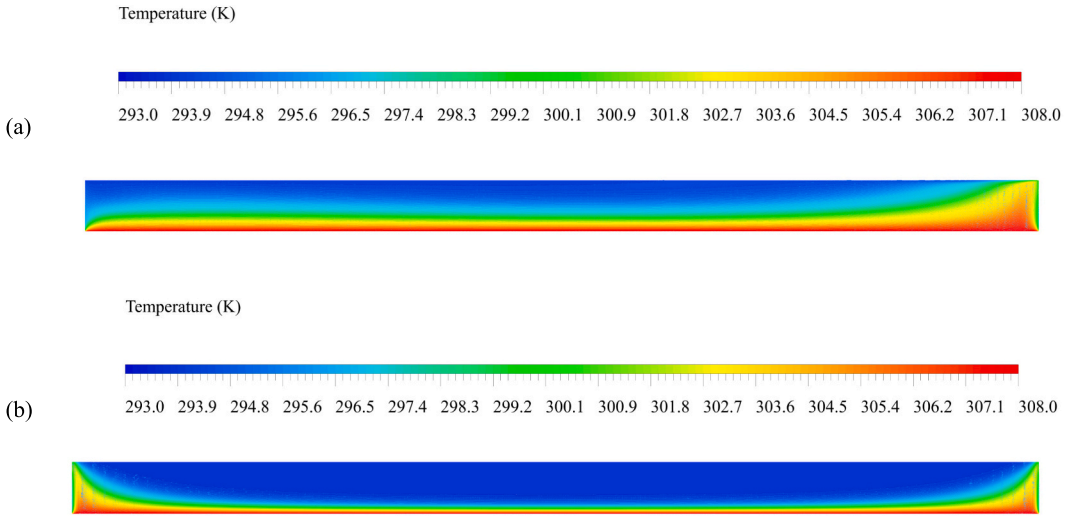

Fig. 4. Temperature contours for sample S2 at an inlet velocity of 4 m/s under (a) horizontal and (b) vertical wind orientations.

and the configuration is horizontal, increasing the thickness leads to a substantial rise in thermal resistance. For instance, as the thickness increases from S1 to S3, where S3 is approximately 2.18 times thicker than S1, the thermal resistance increases by about 76.5%. However, at a higher velocity of 4 m/s and horizontal configuration, this improvement decreases sharply to only 12.2%, indicating that greater thickness provides limited benefit under stronger wind conditions. In the vertical orientation, the effect is even less favorable; at 1 m/s, the same increase in thickness enhances thermal resistance by only 21.1%, far lower than in the horizontal configuration. This behavior results from the dual influence of thickness: while a thicker layer suppresses conduction, it also creates a larger internal air space that facilitates airflow circulation and

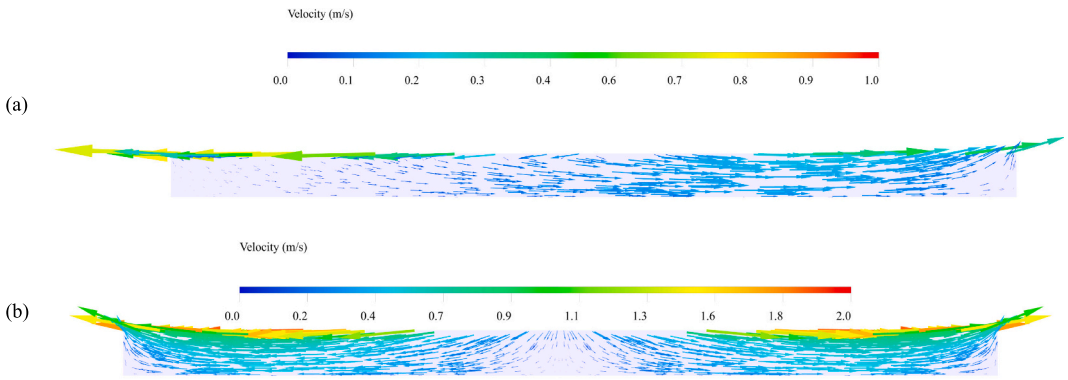

Fig. 5. Velocity vector fields for sample S2 at an inlet velocity of 4 m/s under (a) horizontal and (b) vertical wind orientations.

intensifies convective heat transfer, particularly under vertical or high-velocity wind exposure. As a result, the insulation benefit gained from increased material thickness is gradually offset by enhanced convection within the porous structure. A similar trend has been reported in other studies, where increasing air-layer thickness beyond approximately 10 mm produced negligible gains in thermal insulation due to the formation of internal convection that accelerate heat transfer [24]. Therefore, the effectiveness of adding thickness depends on maintaining a proper balance between reducing conductive heat flow and limiting internal air movement. The observed interdependence among thickness, wind orientation, and velocity underscores the need to evaluate the individual heat-transfer mechanisms, as discussed in the following section.

3.4. Contribution of heat transfer modes

The relative contributions of conduction, convection, and radiation for the three fabric structures (S1–S3) under different inlet velocities are shown in Fig. 7 (a–c). Each figure compares horizontal and vertical configurations to illustrate the combined influence of wind orientation and fabric thickness on heat-transfer mechanisms. At a low velocity of 1 m/s (Fig. 7 (a)), conduction dominates the horizontal configuration, contributing 68.4–79.7% of the total heat flux, highest for the thinnest sample (S1) and lowest for the thickest (S3). Radiation contributes 11.3–14%, emphasizing an important distinction from Shen et al. [20], who did not account for radiative transfer in their analysis of similarly porous structures. Meanwhile, convection rises from 6.2% in S1 to 20.3% in S3, confirming that greater thickness facilitates air movement within the textile assembly. In the vertical configuration, even at 1 m/s, convection already surpasses conduction in samples S2 and S3, reinforcing that increasing thickness is not an effective strategy for improving thermal resistance when airflow penetrates the structure. As the inlet velocity increases to 2 m/s (Fig. 7(b)), convective heat transfer intensifies in both orientations. Considering vertical configuration, for S1, convection becomes comparable to conduction, whereas in S2 and S3, it becomes the dominant mode of heat transfer. At 4 m/s (Fig. 7(c)), convection governs the process almost entirely, reaching 86.2% of the total heat flux in the vertical configuration of S3. In this case, conduction decreases to approximately 11.9%, and radiation falls to 1.9%, demonstrating that reducing radiative exchange has negligible impact under windy conditions. Overall, these results reveal that wind velocity, orientation, and structural thickness critically determine the heat-transfer regime. Conduction prevails under low-velocity or horizontal flow conditions, but convection rapidly becomes dominant with increasing velocity and vertical orientation. Therefore, enhancing insulation performance in such fabrics should focus on minimizing air permeability, while still allowing adequate water-vapor transmission to maintain wearer comfort.

3.5. Effect of wind velocity on the thermal resistance of the thinnest structure (S1)

The variation of thermal resistance for the thinnest nonwoven structure (S1) under inlet wind velocities up to 32 m/s is shown in Fig. 8 for the vertical configuration. This structure was selected for detailed analysis based on the results presented in Section 3.3, where its thermal resistance under a 4 m/s vertical flow was only 9.9% lower than that of the thickest sample (S3), despite S3 being 2.18 times thicker. This indicates that S1 provides comparable insulation with substantially lower material usage, an advantage for lightweight cold-protective clothing. As shown in Fig. 8, the thermal resistance decreases markedly with increasing wind velocity. At low velocities, the initial penetration of air into the porous network enhances convective heat transfer, leading to a sharp reduction in overall resistance. With further increases in wind speed, convective heat transfer progressively dominates over conduction and radiation. By the time the wind speed reaches the regime where convective effects would be dominant, additional increases in wind velocity result in only marginal changes in heat flux, and the thermal resistance gradually stabilizes. This behavior results in the characteristic nonlinear trend observed in Fig. 8, a steep decline at low wind velocities followed by a near-plateau at higher speeds. A similar trend was reported by Shen et al. [20], who examined a nonwoven structure with approximately 99% porosity and comparable air permeability under horizontal wind exposure up to 35 m/s, reinforcing the consistency of the observed wind velocity effects on thermal resistance in highly porous textile assemblies.

3.6. Effect of air permeability on the thermal resistance of the S1 structure

The influence of air permeability on the thermal resistance of the thinnest fabric structure (S1) under a vertical wind velocity of 4 m/s was investigated, as shown in Fig. 9. The lowest permeability case (0.1×10^{-7} m^2) corresponds to a configuration where the structure exhibits flow resistance in both x and y directions comparable to that of a sample covered with a thin cotton film (0.089×10^{-7} m^2). As illustrated, reducing air permeability markedly increases thermal resistance, up to 2.83 times higher than that of the reference S1 structure. Conversely, increasing permeability to levels similar to a film-free structure (200×10^{-7} m^2) in both x and y directions results in a 37% reduction in thermal resistance (0.63 × the baseline value). This demonstrates the significant role of the film layer in suppressing convective heat loss through the fabric assembly. Although minimizing air permeability enhances insulation by suppressing convective heat transfer, excessively low permeability is undesirable for clothing applications since it restricts water-vapor transmission and compromises comfort. Notably, even an idealized structure with an air permeability only twice that of the film-covered case (0.2×10^{-7}) would still yield a 2.3-fold improvement in thermal resistance compared to the standard S1 sample. This finding

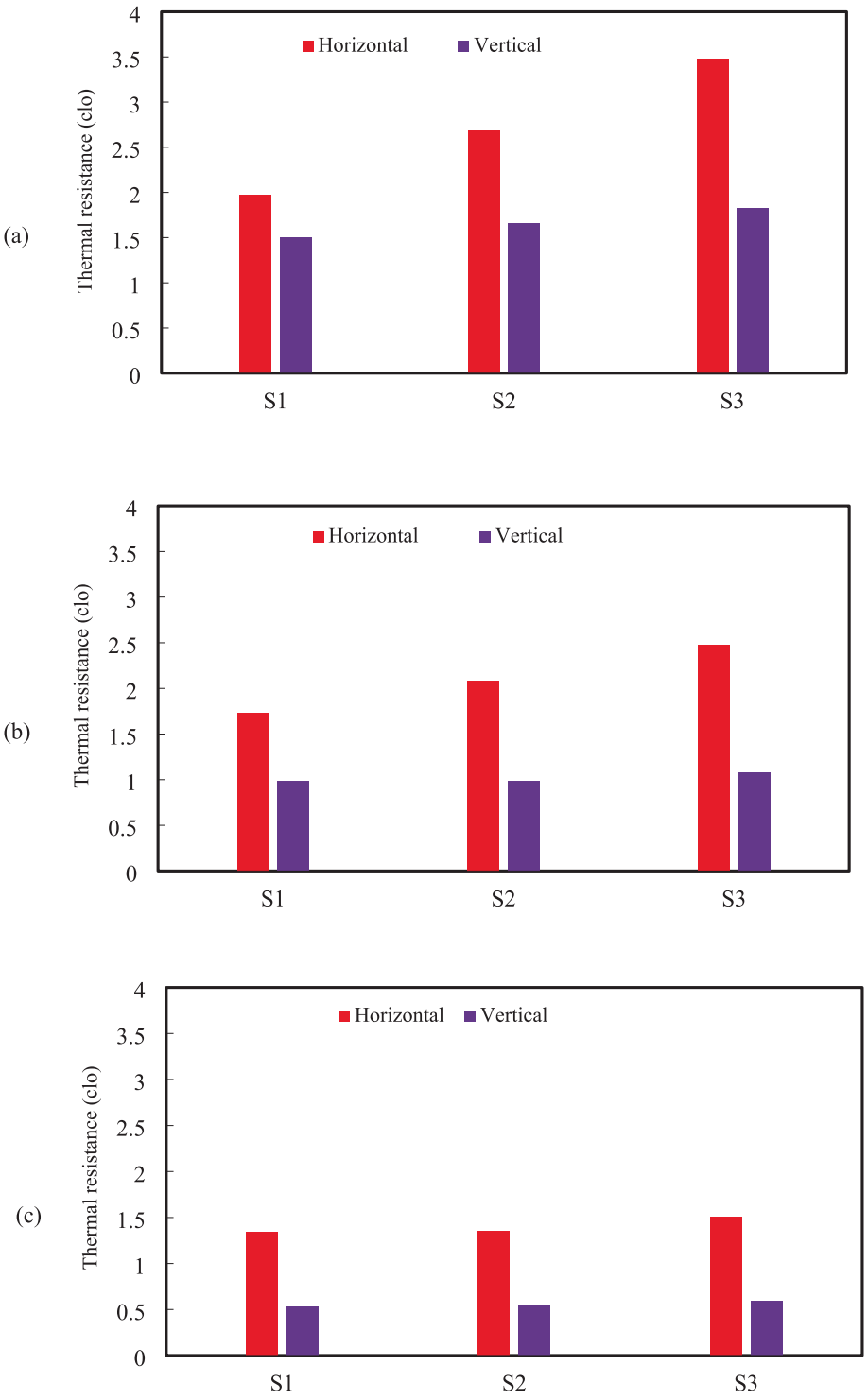

Fig. 6. Thermal resistance of samples S1–S3 under (a) 1 m/s, (b) 2 m/s, and (c) 4 m/s inlet velocities for both horizontal and vertical configurations.

underscores the importance of optimizing permeability, rather than minimizing, to achieve a balance between thermal protection and moisture management in cold-protective nonwoven fabrics.

4. Conclusion

This study provided a comprehensive numerical investigation into the thermal resistance of multi-component nonwoven structures designed for cold-protective clothing. By examining structural parameters such as fiber hollowness, fabric porosity, and air permeability under various wind intensities and orientations, the results emphasize that optimal design requires balancing permeability, thickness, and fiber structure to minimize convective heat loss while preserving wearer comfort. Based on this analysis, the following main conclusions were drawn:

- Numerical framework and validation: a 2D computational framework was developed based on the porous-media approach, which integrates the pressure drop caused by the fibrous network as sink terms in the momentum equations. The flow outside the textile was

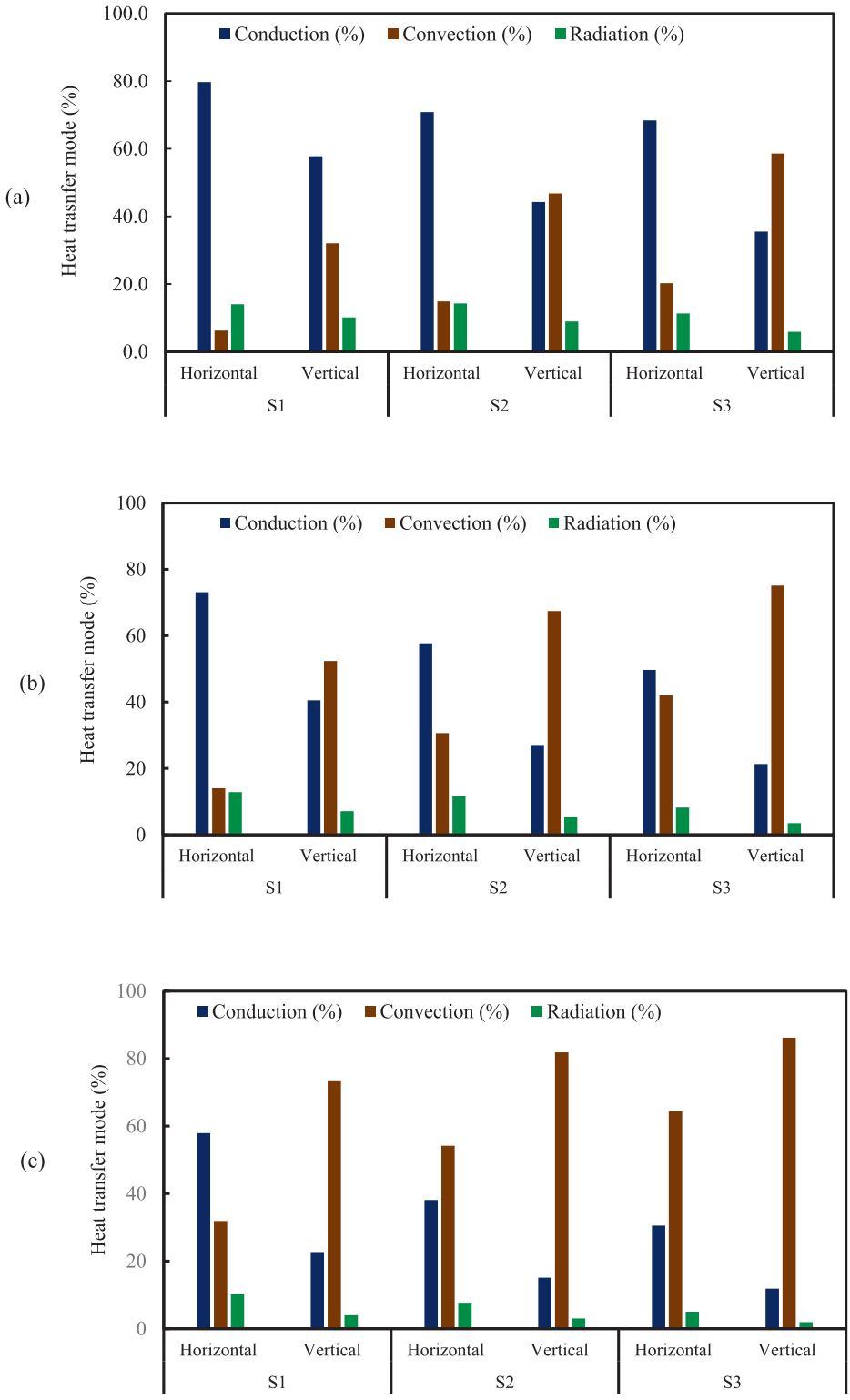

Fig. 7. Relative contributions of conduction, convection, and radiation for samples S1–S3 under (a) 1 m/s, (b) 2 m/s, and (c) 4 m/s inlet velocities in both horizontal and vertical configurations.

treated as turbulent using the k–ω SST model, whereas the internal flow was modeled as laminar. The energy equation assumed local thermal equilibrium but was modified to account for multicomponent fiber composition, fiber hollowness, and radiative heat transfer. Model reliability was verified by comparing simulated and experimental thermal resistances of sample S2, showing good agreement with maximum deviations of 18.6% (horizontal) and 20.2% (vertical).

- Heat transfer mechanisms: analysis of individual heat-transfer modes confirmed that conduction dominates under mild airflow. Conversely, convection becomes the governing mechanism as wind velocity and exposure angle increase, while radiative heat transfer contributes less than 1.9% at high wind speeds.

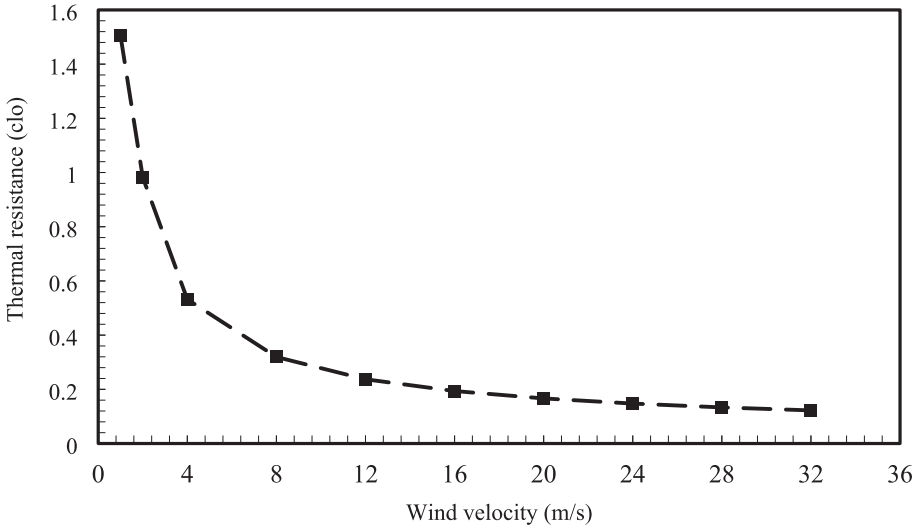

Fig. 8. Variation of thermal resistance of the S1 structure with inlet wind velocity for vertical configuration.

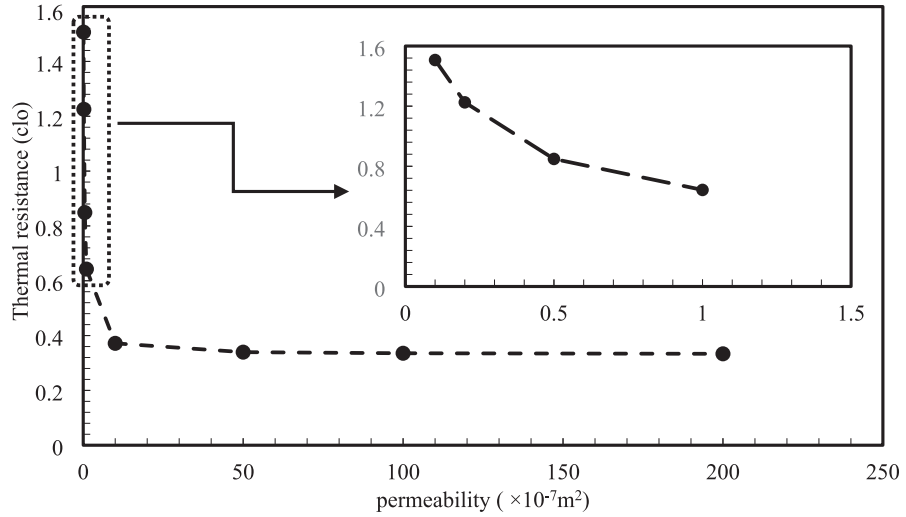

Fig. 9. Variation of thermal resistance of the S1 structure with air permeability under vertical wind velocity of 4 m/s.

- Influence of thickness and orientation: the influence of thickness was analyzed using samples S1–S3. Increasing fabric thickness enhances thermal resistance primarily under low-velocity, horizontal wind conditions. However, this benefit diminishes at higher velocities or under vertical wind exposure due to the onset of enhanced internal convection.
- Velocity dependence: testing of the thinnest structure (S1) up to 32 m/s revealed that thermal resistance decreases nonlinearly with velocity. The resistance falls sharply at low wind speeds and stabilizes once convection reaches a steady state.
- Role of permeability: lowering air permeability significantly enhances insulation, reaching up to 2.83 times the baseline. However, air permeability should be optimized rather than simply reduced, as excessive reduction hinders water-vapor transmission and compromises wearer comfort.

CRediT authorship contribution statement

Seyyed Mohsen Mortazavinejad: Writing – original draft, Software, Methodology, Investigation, Data curation. **Ludwig Vinches:** Writing – review & editing, Supervision, Project administration, Investigation. **Stéphane Hallé:** Writing – review & editing, Supervision, Investigation, Conceptualization.

Declaration of generative AI and AI-assisted technologies in the writing process

During the preparation of this work, the authors used ChatGPT-4 in order to improve readability and language. After using this tool, the authors reviewed and edited the content as needed and take full responsibility for the content of the publication.

Declaration of competing interest

The authors declare that they have no known competing financial interests or personal relationships that could have appeared to influence the work reported in this paper.

Acknowledgements

This work was supported by a financial support of our industrial partners, Logistik Unicorp Inc. and Eko-Terre, as well as a grant from PRIMA Québec (N° R23-13-001) and the Natural Sciences and Engineering Research Council of Canada (ALLRP 566738 - 21).

Data availability

Data will be made available on request.

References

[1] ISO 15743, Ergonomics of Thermal Environment - Cold Workplaces - Risk Assessment and Management, Science and Technology of Nuclear Installations, 2008.

[2] H. Hensel, Thermoreception and temperature regulation, Monogr. Physiol. Soc. 38 (1981), https://doi.org/10.1016/0306-4565(91)90010-y.

[3] A. Das, R. Alagirusamy, Science in Clothing Comfort, Woodhead, 2010, https://doi.org/10.1533/9780857092830.

[4] A. Patnaik, M. Mvubu, S. Muniyasamy, A. Botha, R.D. Anandjiwala, Thermal and sound insulation materials from waste wool and recycled polyester fibers and their biodegradation studies, Energ. Buildings 92 (2015) 161–169, https://doi.org/10.1016/j.enbuild.2015.01.056.

[5] A.M. Papadopoulos, State of the art in thermal insulation materials and aims for future developments, Energ. Buildings 37 (1) (2005), https://doi.org/10.1016/j.enbuild.2004.05.006.

[6] H. Shen, A. Yokoyama, S. Sukigara, Modeling of heterogeneous heat transfer in fabrics, Text. Res. J. 88 (10) (2018) 1164–1172, https://doi.org/10.1177/0040517517698986.

[7] V. Fiore, G. Di Bella, A. Valenza, Effect of sheep wool fibers on thermal insulation and mechanical properties of cement-based composites, J. Nat. Fibers 17 (10) (2020), https://doi.org/10.1080/15440478.2019.1584075.

[8] S.B. Stanković, D. Popović, G.B. Poparić, Thermal properties of textile fabrics made of natural and regenerated cellulose fibers, Polym. Test. 27 (1) (2008), https://doi.org/10.1016/j.polymertesting.2007.08.003.

[9] K. Manohar, A. Adeyanju, A comparison of banana fiber thermal insulation with conventional building thermal insulation, Br. J. Appl. Sci. Technol. 17 (3) (2016), https://doi.org/10.9734/bjast/2016/29070.

[10] L.F. Liu, et al., The Development History and Prospects of Biomass-based Insulation Materials for Buildings, 2017, https://doi.org/10.1016/j.rser.2016.11.140.

[11] M.R. Ponnada, K. P, Construction and demolition waste management – a review, Int. J. Adv. Sci. Technol. 84 (2015), https://doi.org/10.14257/ijast.2015.84.03.

[12] C.S. Boland, R. De Kleine, G.A. Keoleian, E.C. Lee, H.C. Kim, T.J. Wallington, Life cycle impacts of natural fiber composites for automotive applications: effects of renewable energy content and lightweighting, J. Ind. Ecol. 20 (1) (2016), https://doi.org/10.1111/jiec.12286.

[13] D. Illera, J. Mesa, H. Gomez, H. Maury, Cellulose aerogels for thermal insulation in buildings: trends and challenges, Coatings (2018), https://doi.org/10.3390/coatings8100345.

[14] X. Lian, L. Tian, Z. Li, X. Zhao, Thermal conductivity analysis of natural fiber-derived porous thermal insulation materials, Int. J. Heat Mass Transf. 220 (2024), https://doi.org/10.1016/j.ijheatmasstransfer.2023.124941.

[15] D. Csanády, O. Fenyvesi, B. Nagy, Heat transfer in straw-based thermal insulating materials, Materials 14 (16) (2021), https://doi.org/10.3390/ma14164408.

[16] R. El-Sawalhi, J. Lux, P. Salagnac, Estimation of the thermal conductivity of hemp based insulation material from 3D tomographic images, Heat Mass Transf. 52 (8) (2016), https://doi.org/10.1007/s00231-015-1674-4.

[17] R. Stapulionienė, S. Vaitkus, S. Vėjelis, A. Sankauskaitė, Investigation of thermal conductivity of natural fibres processed by different mechanical methods, Int. J. Precis. Eng. Manuf. 17 (10) (2016), https://doi.org/10.1007/s12541-016-0163-0.

[18] U. Hammerschmidt, J. Hameury, R. Strnad, E. Turzó-Andras, J. Wu, Critical review of industrial techniques for thermal-conductivity measurements of thermal insulation materials, Int. J. Thermophys. 36 (7) (2015), https://doi.org/10.1007/s10765-015-1863-x.

[19] S.M. Mortazavinejad, M. Alakhdar, L. Vinches, S. Hallé, A novel methodology for calculating thermal conductivity of natural hollow fibers with validation in nonwoven fabric structures, Int. Commun. Heat Mass Transf. 167 (2025) 109269, https://doi.org/10.1016/j.icheatmasstransfer.2025.109269.

[20] H. Shen, Y. Xu, F. Wang, J. Wang, L. Tu, Numerical analysis of heat and flow transfer in porous textiles - influence of wind velocity and air permeability, Int. J. Therm. Sci. 155 (2020), https://doi.org/10.1016/j.ijthermalsci.2020.106432.

[21] G. Zhu, D. Kremenakova, Y. Wang, J. Militky, R. Mishra, J. Wiener, 3D numerical simulation of laminar flow and conjugate heat transfer through fabric, Autex Res. J. 17 (1) (2017), https://doi.org/10.1515/aut-2015-0052.

[22] M. Venkataraman, R. Mishra, J. Militky, B.K. Behera, Modelling and simulation of heat transfer by convection in aerogel treated nonwovens, J. Text. Inst. 108 (8) (2017), https://doi.org/10.1080/00405000.2016.1255124.

[23] S.R. Wang, C.A. Wang, Numerical simulation of convective heat transfer in packed bed using open-source computational fluid dynamics, Powder Technol. 422 (2023), https://doi.org/10.1016/j.powtec.2023.118452.

[24] L. Tu, et al., Numerical investigation of heat transfer and fluid motion in air inflatable textiles: effect of thickness, surface emissivity and ambient temperature, Build. Environ. 225 (2022), https://doi.org/10.1016/j.buildenv.2022.109594.

[25] H. Shen, et al., Influence of windproof layer on heat and mass transfer in porous textiles based on experiment and simulation, Int. Commun. Heat Mass Transf. 142 (2023), https://doi.org/10.1016/j.icheatmasstransfer.2023.106667.

[26] S. Sanchez-Diaz, C. Ouellet, S. Elkoun, M. Robert, Evaluating the properties of native and modified milkweed floss for applications as a reinforcing fiber, J. Nat. Fibers 20 (1) (2023), https://doi.org/10.1080/15440478.2023.2174630.

[27] R.H. Sangalang, Kapok fiber- structure, characteristics and applications: a review, Orient. J. Chem. 37 (3) (2021), https://doi.org/10.13005/ojc/370301.

[28] M. Alakhdar, L. Vinches, S. Hallé, Assessing thermal resistance of a nonwoven textile under wind exposure: challenging ISO 9920 with experimental insights, J. Ind. Text. 55 (2025), https://doi.org/10.1177/15280837251328908.

[29] International Organization for Standardization, *ISO 11092:*2014 - *Textiles – Physiological Effects – Measurement of Thermal and Water-vapour Resistance Under Steady-state Conditions (Sweating Guarded-hotplate Test)*, Second ed., 2014 no. December.

[30] R. Arambakam, H.V. Tafreshi, B. Pourdeyhimi, Modeling performance of multi-component fibrous insulations against conductive and radiative heat transfer, Int. J. Heat Mass Transf. 71 (2014), https://doi.org/10.1016/j.ijheatmasstransfer.2013.12.031.

[31] D.A. Nield, A. Bejan, Convection in Porous Media, 2013, https://doi.org/10.1007/978-1-4614-5541-7.

[32] I. Holmér, H. Nilsson, G. Havenith, K. Parsons, Clothing convective heat exchange-proposal for improved prediction in standards and models, in: Annals of Occupational Hygiene, 1999, https://doi.org/10.1016/S0003-4878(99)00057-5.

[33] S. Evans, S. Lardeau, C. Pettinelli, Validation of a turbulence methodology using the SST k-ω model for adjoint calculation, in: 54th AIAA Aerospace Sciences Meeting, 2016, https://doi.org/10.2514/6.2016-0585.

[34] Ashrae, Thermal environmental conditions for human occupancy, in: ANSI/ASHRAE Standard 55-2004 2004, 2004.

[35] H. Shen, et al., 3D numerical investigation of the heat and flow transfer through cold protective clothing based on CFD, Int. J. Heat Mass Transf. 175 (2021), https://doi.org/10.1016/j.ijheatmasstransfer.2021.121305.

[36] M.S. Santos, D. Oliveira, J.B.L.M. Campos, T.S. Mayor, Numerical analysis of the flow and heat transfer in cylindrical clothing microclimates – influence of the microclimate thickness ratio, Int. J. Heat Mass Transfer 117 (2018), https://doi.org/10.1016/j.ijheatmasstransfer.2017.09.102.

[37] H.C. Brinkman, The viscosity of concentrated suspensions and solutions, J. Chem. Phys. 20 (4) (1952), https://doi.org/10.1063/1.1700493.

[38] T. Dong, F. Wang, G. Xu, Theoretical and experimental study on the oil sorption behavior of kapok assemblies, Ind. Crop. Prod. 61 (2014) 325–330, https://doi.org/10.1016/j.indcrop.2014.07.020.

[39] V. Dupade, R. Kumari, B. Premachandran, R.S. Rengasamy, P. Talukdar, Effect of layering sequence and ambient temperature on thermal insulation of multilayer high bulk nonwoven under extreme cold temperatures, J. Ind. Text. 51 (2_suppl) (2022), https://doi.org/10.1177/15280837221097284.

[40] S. yuan Zhao, B. ming Zhang, X. dong He, Temperature and pressure dependent effective thermal conductivity of fibrous insulation, Int. J. Therm. Sci. 48 (2) (2009), https://doi.org/10.1016/j.ijthermalsci.2008.05.003.

[41] B. Farnworth, Mechanisms of heat flow through clothing insulation, Text. Res. J. 53 (12) (1983) 717–725, https://doi.org/10.1177/004051758305301201.